POLISH POLAR RESEARCH
vol. 37, no. 3, pp. 337–360, 2016 doi: 10.1515/popore-2016-0018

# Surface currents in the Porsanger fjord in northern Norway

Malgorzata STRAMSKA[1,2*], Andrzej JANKOWSKI[1] and Agata CIESZYŃSKA[2]

[1] *Institute of Oceanology, Polish Academy of Sciences, Powstańców Warszawy 55,*
*Sopot 81-712, Poland*

[2] *Department of Earth Sciences, Szczecin University, Mickiewicza 16, Szczecin 70-383, Poland*
*<mstramska@wp.pl> <jankowsk@iopan.gda.pl> <cieszynska.agata@gmail.com>*

* *corresponding author*

**Abstract**: We describe surface currents in the Porsanger fjord (Porsangerfjorden) located in the European Arctic in the vicinity of the Barents Sea. Our analysis is based on surface current data collected in the summer of 2014 using High Frequency (WERA, Helzel Messtechnik GmbH) radar system. One of our objectives was to separate out the tidal from the nontidal components of the currents and to determine the most important tidal constituents. Tides in the Porsanger fjord are substantial, with tidal range on the order of about 3 m. Tidal analysis attributes to tides about 99% of variance in sea level time series recorded in Honningsvaag. The most important tidal component in sea level data is the M2 component, with amplitude of ~90 cm. The S2 and N2 constituents (amplitude of ~20 cm) also play a significant role in the semidiurnal sea level oscillations. The most important diurnal component is K1 with amplitude of about 8 cm. The most important tidal component in analyzed surface currents records is the M2 component. The second most important component is the S2. Our results indicate that in contrast to sea level, only about 10–30% of variance in surface currents can be attributed to tidal currents. This means that about 70–90% of variance is due to wind-induced and geostrophic currents.

Key words: Arctic, northern Norway, fjords, coastal processes, tides, ocean observing systems.

## Introduction

Fjords are elongated, deep, and narrow bays surrounded by mountains and sea cliffs. They constitute an interface between the land and the ocean. On one hand, they are influenced by the physical and chemical properties of the oceanic boundary currents. A buoyancy-driven estuarine exchange controls the transport of saltier seawater into the fjords. On the other hand, fjords act as export channels for the fresh water runoff from land into the ocean and this can potentially affect the shelf hydrography and biogeochemical properties of oceanic waters. Processes such as geostrophic control, tidal and local wind driven currents can play a significant role in these interactions.

The Porsanger fjord is located at about 25.0–26.5°E and 70.0–71.0°N (Fig. 1a). It is approximately 100 km long, 15–10 km wide, has a maximum depth of more than 230 m, and extends in the southwest direction from the northern tip of Norway in the coastal region of the Barents Sea (Fig. 1b). It has been proposed in the past that if the fjord width significantly exceeds the first baroclinic radius of deformation it should be classified as a broad fjord (Cushman-Roisin *et al*. 1994). In broad fjords, the Coriolis effect leads to upwelling and downwelling responses that are contained within the deformation radius along each side of the fjord that behave like separate coastal regions. Cushman-Roisin *et al*. (1994) have evaluated the Porsanger fjord using this criterion. In their calculations, they have assumed the latitude of 70.5°N ($f = 1.37 \times 10^{-4}\ s^{-1}$), mean depth of $H = 200$ m, mean width of $L = 18$ km, and that a homogeneous upper layer of density $\varrho_1 = 1022$ kg m$^{-3}$ and depth $H_l = 50$ m is located on top of the deep-water layer with average density $\varrho_2 = 1024$ kg m$^{-3}$ and $H_2 = 150$ m. From these assumptions they have derived the reduced gravity $g' = g(\varrho_2 - \varrho_1)/\varrho_2 = 0.02$ m s$^{-2}$ and the baroclinic radius of deformation $R = (g' H_l H_2 / H)^{1/2}/f = 6.3$ km. Thus, according to Cushman-Roisin *et al*. (1994), the width of the Porsanger fjord is approximately three times the deformation radius, and the fjord can be classified as an intermediate size.

Since the freshwater input from land to fjords is a major factor controlling their hydrography including water circulation, Svendsen (1995) suggested a classification of fjords based on the ratio of water runoff to the surface area of a fjord. This allows one to classify fjords into three broad categories: (i) fjords with relatively small freshwater runoff where wind stress is a key forcing mechanism for the water circulation, (ii) fjords with relatively large runoff, where density currents dominate the hydrography, (iii) fjords with intermediate water runoff. The Porsanger fjord has been classified as a fjord with relatively low runoff, but in the spring/summer season freshwater runoff can significantly influence its hydrography.

Based on topography, the Porsanger fjord (Fig. 1b) can be divided into three different zones: inner (0–30 km), middle (30–70 km), and outer (70–100 km). The inner zone is separated from the remainder of the fjord by the 60-m deep sill, situated approximately 30 km from the inland end (head) of the fjord. The middle part of the fjord starts outside of this sill, and is separated from the outer zone by an island (Tamsøya) located about 70 km from the head of the fjord. The outer zone ends with a deep sill (180 m), therefore it is well connected with the coastal water masses of the Barents Sea. This is in contrast to the inner part of the fjord, which has quite limited exchange with the open sea and is undergoing strong cooling during most of the year. In this inner zone, the

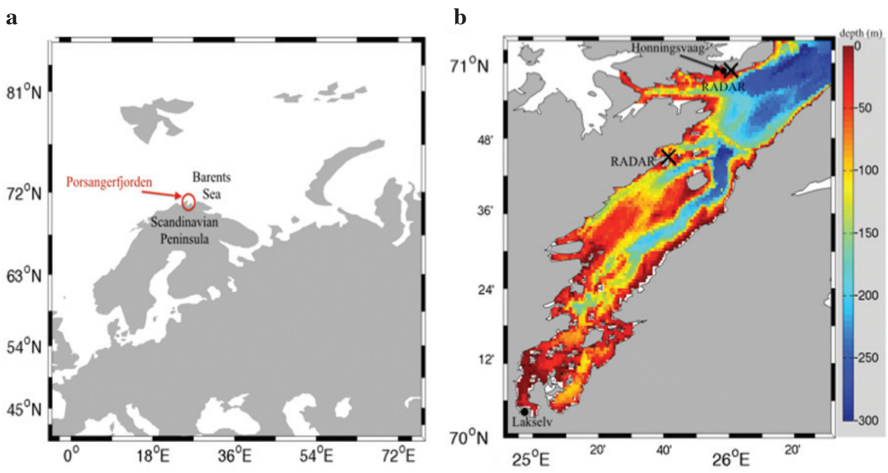

Fig. 1. Location of the Porsanger fjord in the northern Europe (**a**) and its bathymetry (**b**). Positions of the HF radars are indicated by exes.

environment is very different from the rest of the fjord and holds a unique arctic ecosystem (Eilertsen and Frantzen 2007). The Porsanger fjord is stratified from May to October due to seasonal river runoff and surface heating (Svendsen 1995).

In this paper, we describe surface currents in the outer zone of the Porsanger fjord. Our analysis is based on data collected in the summer of 2014. Our interest in this fjord comes from the fact that this is a region of high climatic sensitivity. For example, it has been documented that sea surface temperature (SST) has increased in this area of the Barents Sea at a rate of 0.04°C to 0.05°C per year (Jakowczyk and Stramska 2014). According to Good *et al*. (2007), the globally averaged SST trend (calculated for 20 years of AVHRR Pathfinder data from January 1985 to December 2004) is only about 0.018°C to 0.017°C per year, thus trends in the coastal region of the Barents Sea are stronger than the global average. In addition, significant changes in the ecosystem of the Porsanger fjord have been observed in recent years (Sivertsen and Bjørge 2015). One of our long-term goals is to develop an improved understanding of the ongoing changes and interactions between the Porsanger fjord and the large-scale atmospheric and oceanic conditions in the Barents Sea.

In order to derive a better understanding of the ongoing changes, one must first improve the knowledge of the basic physical processes that shape the environment of the fjord. The present study is the first step in this direction. One of our objectives is to evaluate the importance of tidal and non-tidal forcing on surface currents. In particular, we will estimate what contribution to the total variance of surface currents can be attributed to tidal and non-tidal variability and we will show which tidal components contribute significantly to the observed surface currents.

## Data sets and methods

The basic data set used in this paper includes vector components of surface currents measured using high frequency (HF) radar system (*e.g.*, Helzel *et al.* 2010, 2011) operating in the Porsanger fjord from June 10, 2014 (year day 161) to October 11, 2014 (year day 284). HF radar systems are unique in their ability to monitor surface patterns of ocean currents, and to provide synoptic current maps over extended periods of time. These systems are now widely accepted by the oceanographic community as an efficient tool and are routinely used by many U.S. and European oceanographic research organizations (see for example the Southern California Coastal Ocean Observing System at www.sccoos.org). The performance of HF radars has been extensively tested by comparisons with moored ADCPs, ship mounted ADCPs, drifters and models (*e.g.*, Carbajal and Pohlmann 2004; Chapman *et al.* 1997; Kaplan *et al.* 2005; Kohut and Glenn 2003; Kokkini *et al.* 2014; Ohlmann *et al.* 2007; Shay *et al.* 2008; Parks *et al.* 2009; Robinson and Wyatt 2011). For example, comparisons of ADCP and WERA (Wellen Radars) estimates of surface currents at the observation network in the German Bight showed that the standard deviation between the two estimates was less than 0.1 $ms^{-1}$ and the bias was -0.004 $ms^{-1}$. Chapman *et al.* (1997) pointed out that, since HF radar noise is random, standard errors decrease as the length of the time series increases.

WERA system applied in this study has been developed at the University of Hamburg in 1996, and demonstrated robust accuracy and reliability at numerous installation sites (*e.g.*, Helzel *et al.* 2010, 2011; Kokkini *et al.* 2014). In our experiment, WERA system was used in a phased-array mode, advantageous in fjord environment where spatial and temporal variability of surface currents is relatively high. An in-depth overview of HF radars can be found for example in Paduan and Graber (1997). We will only summarize here the most important aspects, for completeness. In our application, the system used 4 transmit and 12 receive antennas, HF frequencies were set to about 26 MHz and the nominal bandwidth was 250 kHz. The method uses the observations of Doppler (*i.e.* frequency) shift between the transmitted and received radiowave signals to infer the total sea surface velocity. The knowledge about Bragg scattering is applied to remove the influence of sea surface waves and to calculate the horizontal velocity of the current. Bragg scattering, geometric resonance phenomenon, leads to a much stronger signal at the receiver from the Bragg-resonant sea surface waves than from any other constituent of the sea surface wave field. Recall that, according to the deep-water theory for gravity waves, wind driven ocean waves with wavelengths comparable to the electromagnetic wavelengths in the HF band move at a precisely known speed depending only on the wavelength itself. Removal of that speed from the total speed determined from the Doppler shift of the backscattered radiowaves results in estimates of the ocean current velocity. This implies, that the measurements of surface currents with HF radars are restricted to the depth of the Bragg-resonant wind-waves. These waves decay exponentially with depth from the sea surface. Therefore, radar-derived ocean currents in our experiment represent the surface water layer approximately 0.5 m deep.

Another critical aspect of surface current mapping with HF radars is the fact that each instrument (radar) produces a map of ocean current velocity components along radial lines emanating from the radar site. At least two radar sites are needed to derive full velocity vectors of the currents. The installation in the Porsanger fjord included two transmit (Tx) and receive (Rx) sites positioned at about 27 km from each other. Radar stations were located in Repvaag (70.76°N, 25.69°E) and Nordvaagen (70.97°N, 26.02°E), as indicated in Fig. 2. The region monitored by the radars is located in the outer zone of the the Porsanger fjord. The positions of several pixels that will be referred to in the Results sections are indicated in Fig. 2 by numbers 1–7 as well as symbols A1, A2, A3 and M. The two-dimensional surface current velocity vectors have been computed by combining the radial velocity components obtained from the two radar stations in the area of signal overlap, using software provided by the manufacturer (Helzel Messtechnik GmbH). The processing steps involved in WERA HF radars data processing are described in detail in the literature (*e.g.*, Barth *et al*. 2010; Stanev *et al*. 2014).

After the transformation of the measurements from radar coordinates (*i.e*. range and azimuth) to Cartesian grid, the spatial resolution of the current vector field was 0.75 km, as shown in Figs 2 and 3. Surface current maps have been provided every half an hour. The HF radar measurement is sensitive to weather conditions, ionospheric reflection, sea-surface conductivity as well as noise from interference, which leads to gaps in the time series after removal of erroneous data. The percentage of high quality data during our experiment in each grid point is shown in Fig. 3a. Note that in the central region about 90% or more good data have been obtained. Near the boundaries of the monitored area the record exhibits a radial decrease in data return, thus reducing data availability in distant areas. Preliminary data processing has been performed on full resolution 30-minute data record by the WERA software. During this process the quality control has been performed on raw data. After the final data processing, the 2D flow data are referred to as total vectors and contain u (east–west) and v (north–south) velocity components at each grid point. The missing current components have been interpolated in space by the WERA software to fill in small data gaps (one or two records missing). After this interpolation the number of missing data slightly increased as shown in Fig. 3b. In addition to values of surface current vector components, the processed HF radar data set includes estimates of the accuracy for each component (*e.g*., Stanev *et al*. 2014). This accuracy estimate includes the influence of the geometry between

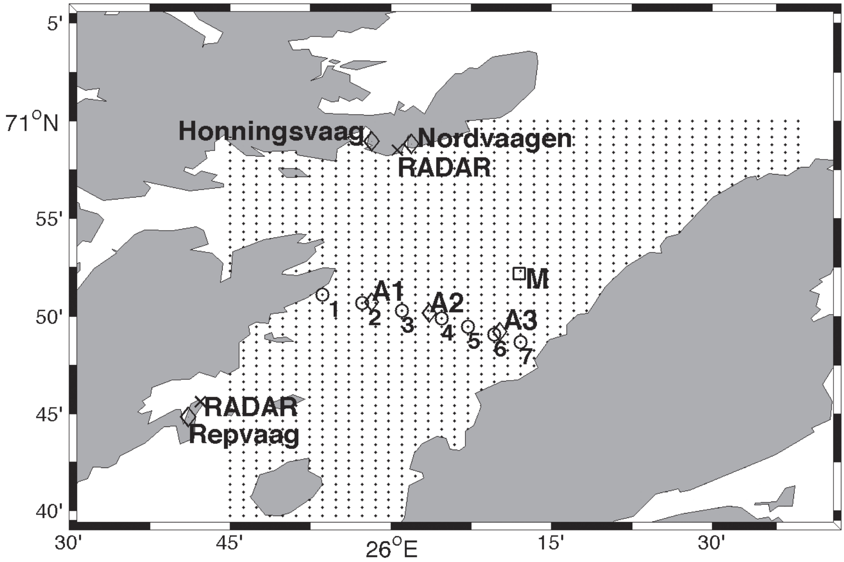

Fig. 2. Spatial grid used for the HF radar measurements. HF radar stations were deployed in Nordvaagen and Repvaag. The letters A1, A2, A3, and M indicate the locations discussed in the text. Time series of surface current data from these pixels are presented in Results and interpretation section. Numbers 1–7 indicate stations S included in the diagram shown in Fig. 16. Sea level and meteorological data were recorded in Honningsvaag (from the Norwegian Meteorological Institute and the Norwegian Mapping Authority, Hydrographic Service).

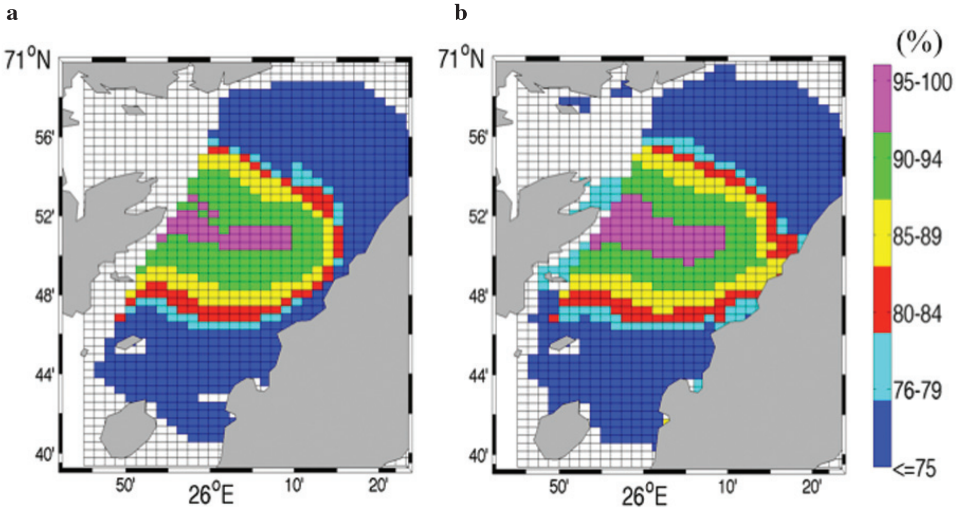

Fig. 3. Availability of HF radar-measured current vectors during the time period of June 10, 2014 to October 11, 2014, (**a**) percentage of data return when both vector components were recorded, (**b**) percentage of data return when interpolated data for one vector component are additionally included in the estimate.

the radar sites and random errors. The accuracy of 99% of recorded u and v component data was below 0.04 $ms^{-1}$ and 0.035 $ms^{-1}$ at pixels discussed in this paper. Harmonic analysis described below was done on uninterpolated, subsampled data sets with hourly resolution and we have focused on the region where data coverage shown in Fig. 3a was 90% or more. Before this analysis, a small number of outliers that differed from average values by more than 3 standard deviations was removed.

Additional data sets have also been used. Sea level data were provided by the Norwegian Hydrographic Service through their websites (http://kartverket.no and http://vannstand.no). We have carried out tidal analysis using the 19-year long time series (1996–2014) of sea level data from Honningsvaag (70.980°N, 25.972°E). Meteorological data from Honningsvaag with hourly resolution covering the time period from June to October 2014 were obtained from the Norwegian Meteorological Institute (http://www.yr.no). The geographical location of Honningsvaag is shown in Fig. 2.

In order to derive an understanding of the temporal and spatial patterns of surface currents in the Porsanger fjord, we have carried out tidal analysis of sea level and surface current data. The purpose of this analysis was to separate out the tidal from the nontidal components of the currents and to determine the most important tidal constituents. The underlying assumption of tidal analysis is that tidal oscillations can be broken down into a collection of simple sinusoids. Although the real ocean is generally not in equilibrium with tidal forcing, tidal amplitudes are small compared with the total ocean depth in many regions. In such a scenario, the dynamics are nearly linear, the forced response contains only those frequencies present in the forcing, and specialized analysis techniques can be used to take advantage of the deterministic nature of tidal processes.

For our calculations, we have used the method based on a least-squares fit coupled with nodal modulation for the constituents that can be resolved over the length of a given data record. The method has been described in detail by Foreman (1977, 1978). The computer codes with manuals are available at www.pac.dfo-mpo.gc.ca/science/oceans/tidal-marees/index-eng.html. Two sets of harmonic tidal analyses were performed. In the first case, the analysis was carried out for the 19-year long time series of sea level (1996–2014). In the second case, the tidal analysis was completed for surface currents. In this case, the data from our field measurements covering the time period from June 10 to October 11, 2014 have been used.

Errors in the tidal current analysis can result from two major sources. These are the contamination of the harmonic analysis results due to current oscillations not associated with tides and measurement errors in the current data. However, these measurement errors are random in nature rather than systematic, therefore their effect on the harmonic analysis results should be substantially reduced over the record lengths (123 days) used in our analysis. One phenomenon that potentially can have some influence on our results are inertial oscillations, that at the latitudes (~71°N) of our study area have period of 12.67 hours, similar to N2 semi-diurnal tidal constituent. The intensity of inertial oscillations depends on fluctuations in the surface wind. Because individual inertial events have a relatively short duration and occur at random phase with one another, the effect on the results of tidal current analysis is most likely reduced. However it is possible that our estimate of the N2 tidal current component is somewhat overestimated.

In addition to tidal harmonic analysis, we have carried out spectral analysis. Autospectra of physical variables have been determined using standard signal processing techniques (Bloomfield 2000; Bendat and Piersol 2010). We applied a Fourier transform to the autocovariance and to the crosscovariance functions to obtain power spectra and squared coherence of scalar variables. The standard error is 34% in these power spectral estimates. The squared coherence above 0.28 is statistically significant at 95% confidence level. Additionally, vector time series, *i.e.* surface currents and residuals, have been resolved into clockwise (CW) and counterclockwise (CCW) components, and rotary spectra, have been estimated following Gonella (1972). In this case, the individual time series were divided into subsamples consisting of 512 data points, and power spectra were averaged. Before these calculations all data gaps were linearly interpolated, and series with gaps longer than four hours were discarded.

Continuous records of surface currents allowed us to estimate the net transport of surface water out from the inner part of the Porsanger fjord during our experiment. This has been done using data recorded at pixels indicated by numbers 1–7 (Fig. 2). First, each current vector has been decomposed into the component parallel to the transect line and another component perpendicular to the transect line. Next, the time series of the current vector components perpendicular to the transect segments have been used to estimate daily average water transport through each of the sectors limited by pixels 1 through 7. Finally, using the trapezoidal approach, total net daily transport of water has been estimated. In these calculations, we have assumed that the surface layer is 1-m deep.

## Results and interpretation

Example maps of current vectors recorded by the HF radar system are presented in Fig. 4. The direction and magnitude of surface currents varies significantly during a day. Our goal is to analyze these complex patterns monitored at high spatial and temporal resolution with HF radars. We will start with describing a background information that can be derived from long time series of sea level observations. The results from tidal analysis of the 19-year long time series (1996–2014) of sea level data from Honningsvaag are summarized in Table 1. For brevity, only the 7 most important tidal components have been

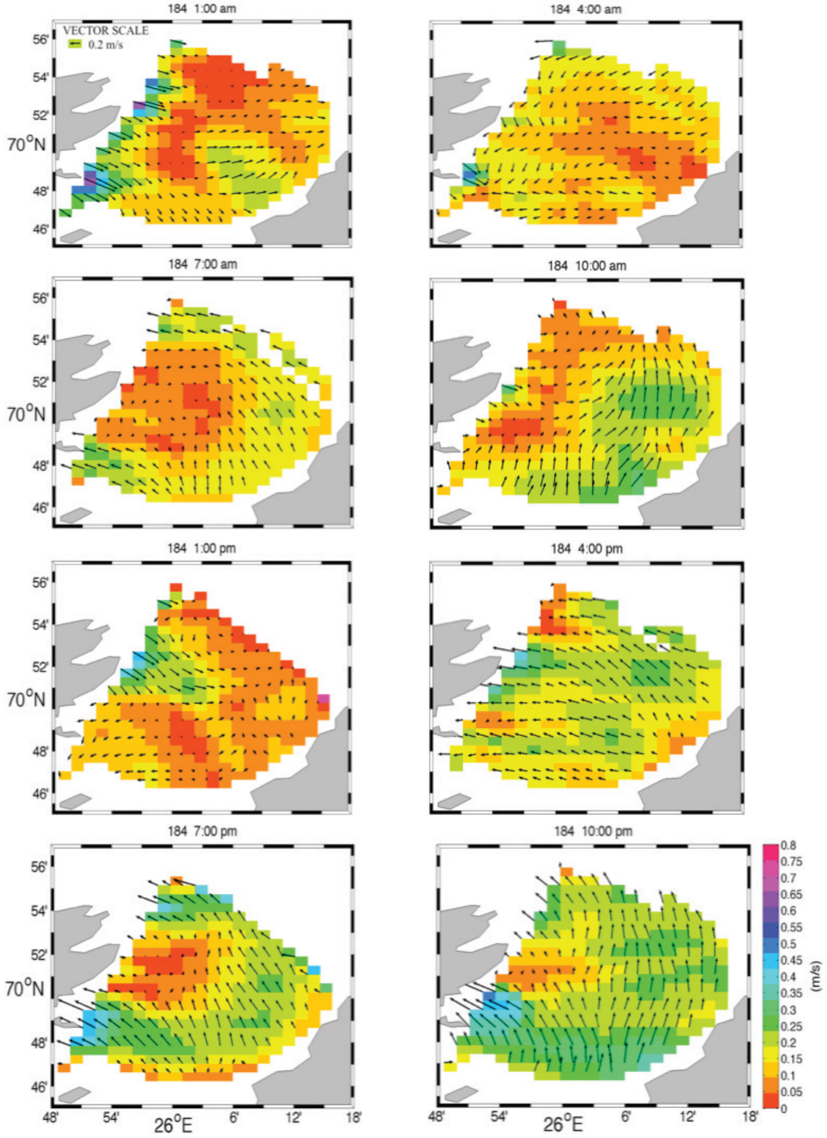

Fig. 4. Example maps showing spatial patterns and temporal variability of surface currents observed during our experiment. This example is for day 184 (July 3, 2014). The lowest sea level on day 184 was recorded at 1 am and 1 pm.

listed in Table 1, but the analysis allowed us to extract 70 components. Figure 5 shows a subset of sea level time series corresponding to the time period covered by our *in situ* experiment (June 10 to October 11, 2014, year days 161–284). The upper panel (Fig. 5a) displays the measured data, the middle panel (Fig. 5b) the modeled tide, and the bottom panel (Fig. 5c) the residual sea level variability.

Table 1

The most important semidiurnal and diurnal tidal constituents estimated from the 19-year long time series of sea level data in Honningsvaag.

| Constituent | Amplitude (cm) | Period (hours) | Phase |
|---|---|---|---|
| M2 | 90.1 | 12.42 | 80.7 |
| S2 | 25.0 | 12.00 | 122.4 |
| N2 | 19.5 | 12.66 | 53.2 |
| L2 | 1.9 | 12.19 | 120.2 |
| K1 | 8.2 | 23.93 | 241.2 |
| O1 | 2.5 | 25.82 | 76.7 |
| P1 | 2.5 | 24.07 | 239.2 |

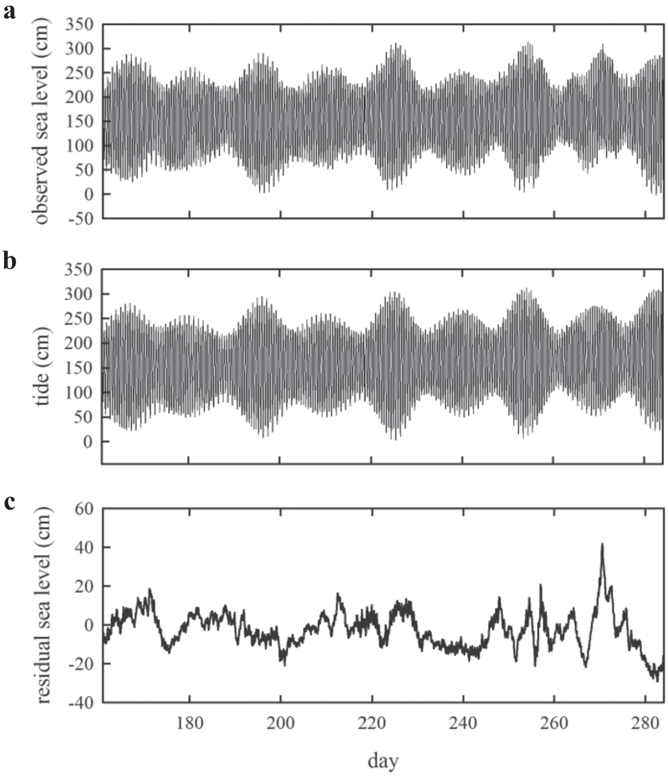

Fig. 5. Subset of time series of sea level recorded in Honningsvaag. This subset covers the time period from June 10, 2014 (year day 161) to October 11, 2014 (year day 284). (**a**) The measured sea level (referenced to the lowest astronomical tide observed at this station). (**b**) The predicted water level variability due to tides. The predicted tidal level is based on the 70 harmonic components obtained from our tidal analysis of the 19 years (1996–2014) of sea level data. The most important components are listed in Table 1. (**c**) The residual sea level estimated as the difference between the measured and the modeled sea level.

Since we have used the data referenced to the lowest astronomical tide, the measured time series are positive numbers. The reconstruction (Fig. 5b) is based on the 70 tidal components determined in the tidal analysis. About 99% of the total variance in the measured time series shown in Fig. 5a is accounted for by the tidal model. The residuals (Fig. 5c) have been estimated as the difference between the measured and the modeled sea level. The residual sea level corresponds to the non-tidal variations in the water level, *e.g.*, due to wind stress or air pressure effects. However, since our reconstruction used limited number (70) of tidal constituents to fit the data, it is also possible that the calculated residuals contain some minor tidal variations not accounted for by the predictive model. We note that the largest residual sea level (about 40 cm) was observed on year day 270.

Figure 6 shows schematically the respective contribution of the six most important diurnal and semidiurnal tidal constituents to the sea level variability in Honningsvaag. Tidal forcing is predominantly semi-diurnal, and the largest constituent is the “principal lunar semidiurnal” indicated by symbol M2 with amplitude of about 90 cm (see Table 1). In addition, we note that the S2 (principal solar semidiurnal) and N2 (larger lunar elliptic semidiurnal) components have amplitudes of about 20 cm, while the most important diurnal constituents have amplitudes of only a few centimeters.

The results from tidal analysis are also presented as diagrams in Fig. 7. Figure 7a shows the reconstructed time series of sea level and Fig. 7b the

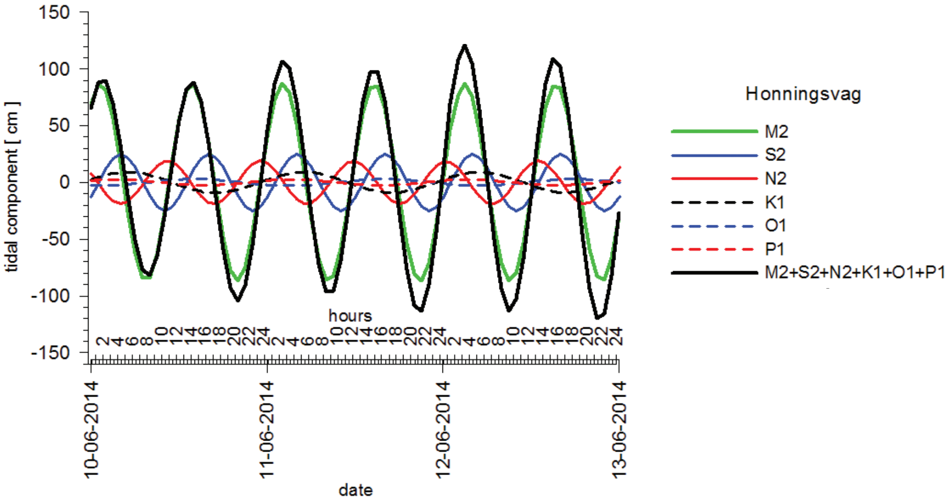

Fig. 6. Relative contribution of the most important tidal components to sea level variability in Honningsvaag.

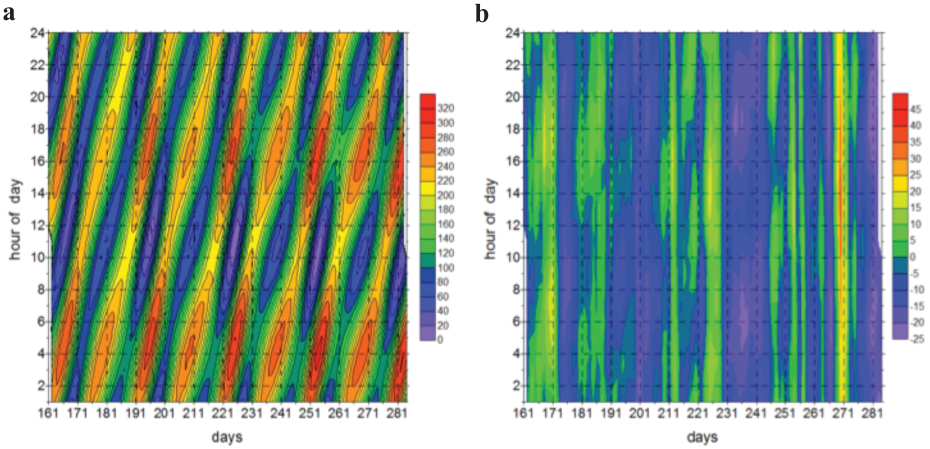

Fig. 7. Diagrams illustrating variability of sea level (in cm) in Honningsvaag during the time period from June 10 (year day 161) to October 11, 2014 (year day 284) due to (**a**) tides (reconstructed) and (**b**) non-tidal contribution (residuals). Note the systematic time shift of the maximum and minimum sea level in panel a.

residual sea levels. Note that hours of each day are shown on the vertical scale and consecutive day numbers are indicated on the horizontal scale of each plot in Fig. 7. This figure allows us to observe how the daily maximum and minimum sea levels shift progressively in time. For example, on day 161 the maximum sea level has been observed at 1–2 am and 1–2 pm. Subsequently, we can observe that the timing of the maximum and minimum sea level gradually shifted during the following days. The tidal amplitude reached for example relatively high values on days 226 and 254, while at other times (days 187, 216) it was much smaller. The highest positive values of residuals are observed on days 270–271 and 170–171, while negative residuals are noted for example on days 281–283 and 235. In order to derive better understanding of the possible factors influencing the magnitudes of the residual sea level variability, we plotted in Fig. 8 time series of meteorological data collected at Honningsvaag airport. Air temperature during our experiment varied mostly between 2 and 15°C, with unusually warm days 187 and 191 (July 6 and 10), when air temperature exceeded 25°C. Wind speed (see Figs 8 and 9) was below 7.5 $ms^{-1}$ most of the time (80%) with some episodes when it exceeded 12.5 m $s^{-1}$ (5% of the time). Wind direction most often varied between north-west to north-east, while the easterly winds were rare (Fig. 9). Comparison of meteorological data with sea level residuals at Honningsvaag station shows that there is an inverse relationship between the sea level residuals and the barometric pressure (Fig. 9d). The correlation coefficient between hourly sea level residuals and barometric pressure is R = -0.74, scatter plot is not shown. The largest residual sea level

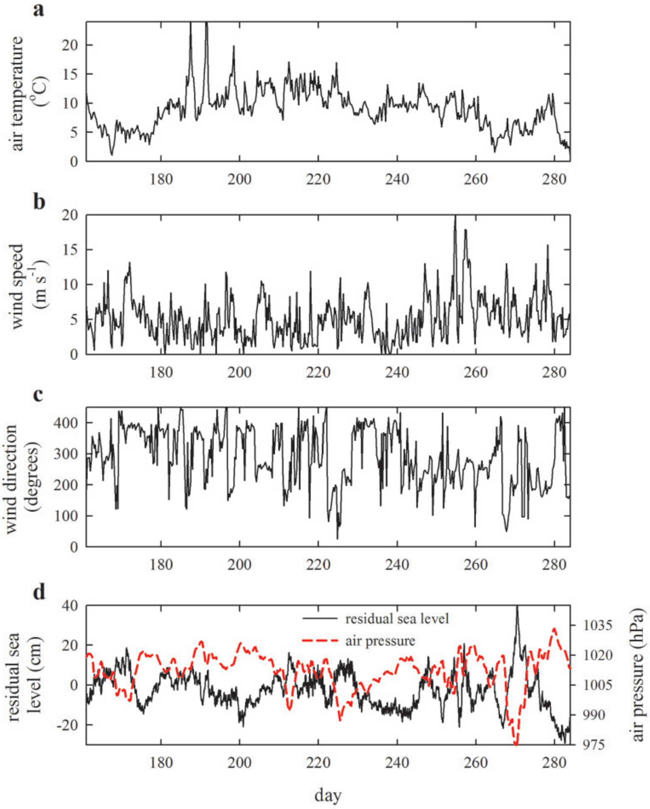

Fig. 8. Meteorological data recorded at Honningsvaag: (**a**) air temperature, (**b**) wind speed, (**c**) wind direction (in meteorological convention, 360 indicates wind from North), and (**d**) atmospheric pressure at sea level and time series of residual sea level. Note, that in situations when the true wind direction oscillated between small and large angles (~50 to 360 degrees) we have added 360 degrees to plot wind direction at small angles in order to make Fig. 8c more readable. This means that, for example, 400 degrees in Fig. 8c indicates the true wind direction of 40 degrees.

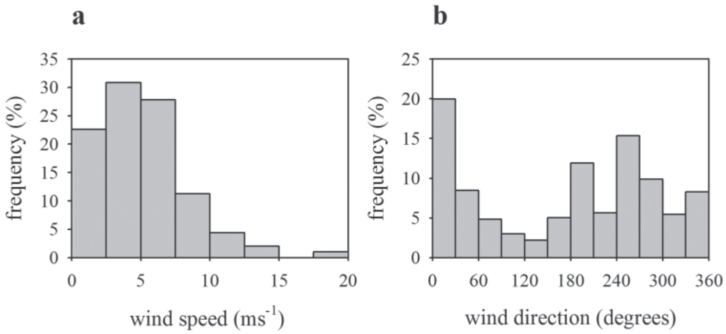

Fig. 9. Frequency distribution of (**a**) wind speed and (**b**) wind direction at Honningsvaag station during our experiment (from June 10 to October 11, 2014).

of about 40 cm was detected on day 270 (September 27, 2014), when the air pressure attained the lowest value observed during our experiment (975 hPa). This relationship between the barometric pressure and sea level is most likely so evident, because sea level station at Honningsvaag is situated in a harbor that is well sheltered from winds. Therefore topographic effects related to wind are minimized at this site.

We will now discuss surface currents, mostly focusing on data representing the pixels highlighted in Fig. 2 (points A1, A2, A3, M, and transect with stations 1–7). Note that the current observed at any time in the ocean is a superposition of tidal and non-tidal components. Tidal current is the periodic horizontal flow of water accompanying the rise and fall of the tide. Nontidal currents include all flows not associated with the tidal movement, for example quasi-permanent geostrophic currents or temporary currents forced by changing meteorological conditions. For instance, inertial ocean currents can play a significant role at our study area, since winds are variable in this region and we observed few events with relatively high winds. Recall, that the inertial currents are the oscillations in water that was set in motion and is moving over a rotating earth. The prime generator of ocean inertial motions is change in wind velocity, but details of the motion depend also on topography and ocean density structure, *e.g.*, Mayer *et al*. (1981). In their simplest form, inertial oscillations are circular motions with the rotation being clockwise in the northern hemisphere. They occur intermittently, as a response to individual wind events, and decay rapidly within a few cycles. The period of inertial oscillations depends on the latitude. The so-called "inertial latitudes" are latitudes where the inertial period is equal to one of the tidal constituents (*e.g*., Wunsch 1975). For the semi-diurnal tidal constituents the inertial latitudes range between 70° and 90°. The period of inertial oscillation in our study region is similar to the semidiurnal period of the dominant tidal forcing (N2 constituent). At stations A1, A2, and A3, the inertial period equals 12.67 hours.

We will focus now our attention on the results of tidal analysis carried out for HF data recoded at pixels 1–7, A1, A2, A3, and M. Example results of analysis for pixels A1 and A3 are shown as time series of measured (Figs 10a and 10c), tidal (Figs 10b and 10e) and non-tidal (Figs 10c and 10f) surface currents. In our analysis, we have estimated the 36 most important tidal constituents. Tidal u and v components of up to about +/- 0.3 $ms^{-1}$ have been observed (Figs 10b and 10e). The magnitudes of the residual current components are generally up to about +/- 0.4 $ms^{-1}$ (Figs 10c and 10f). Figure 11 summarizes the results of tidal analysis for surface currents recorded at pixels S1–S7, see Fig. 2 for positions. Figures 11a and 11b show reconstruction of tidal current components u and v, respectively. Figures 11c and 11d demonstrate u and v components of the residual currents. About 10–30% of the total variance in the measured time series is accounted for by the tidal model. Note that in the offshore locations,

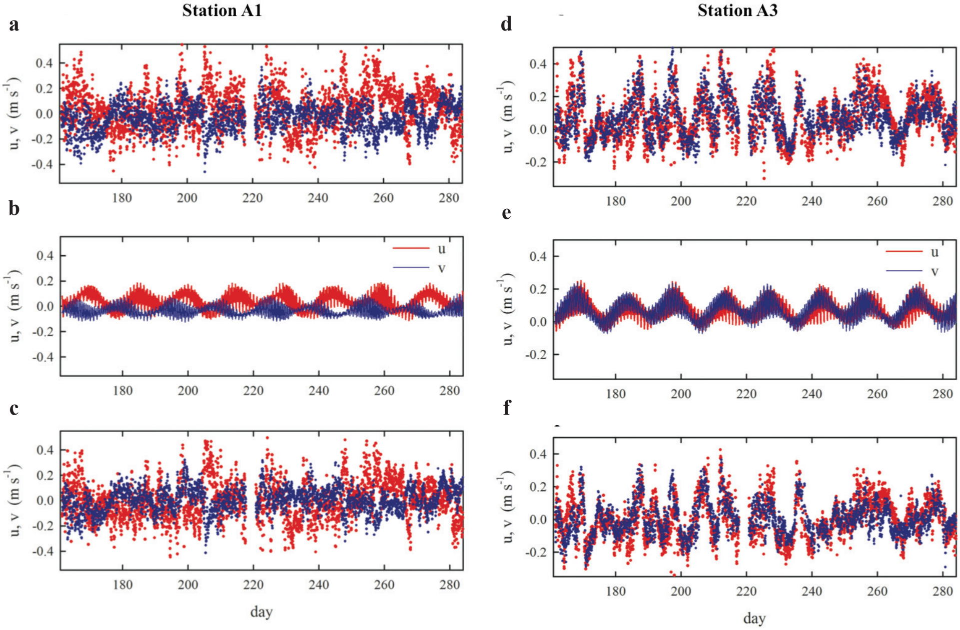

Fig. 10. Example time series of surface currents at pixels A1 and A3: (**a** and **d**) observations, (**b** and **e**) tidal currents (reconstructed), and (**c** and **f**) residual currents estimated as the difference between measured and reconstructed surface currents. Red and blue color indicate u and v current components, respectively.

where the direction of current is not restricted by topography, the tidal currents are rotary. This means that as the current flows, its direction is turning during the entire tidal period through all points of the compass. The speed of the current also changes. Since at our example locations the tidal forcing is predominantly semi-diurnal, current speed usually has two maxima and two minima (at about halfway between the maxima) during the day. The rotary tidal currents can be depicted as the elliptical patterns referred to as current ellipses. The relative importance of the most significant tidal components K1, M2, S2, N2, and L2 at sites A1, A2, A3, and M are compared in Fig. 12. These tidal current ellipses show the length of the semi-major axis and the length of the semi-minor axis. The semi major axis represents the maximum amplitude of the tidal current constituent, while its inclination denotes the angle between the direction of the maximum tidal flow and the true East, in degrees counterclockwise. As can be seen in Fig. 12 and in Table 2, the M2 semidiurnal lunar constituent has the largest amplitude at all sites. The second largest constituent at all points is S2.

Even if 36 major tidal constituents were separated in our tidal current reconstruction, only the M2 constituent will be discussed now since this is the dominant component. In Fig. 13, we present the spatial distribution of the M2 tidal ellipses.

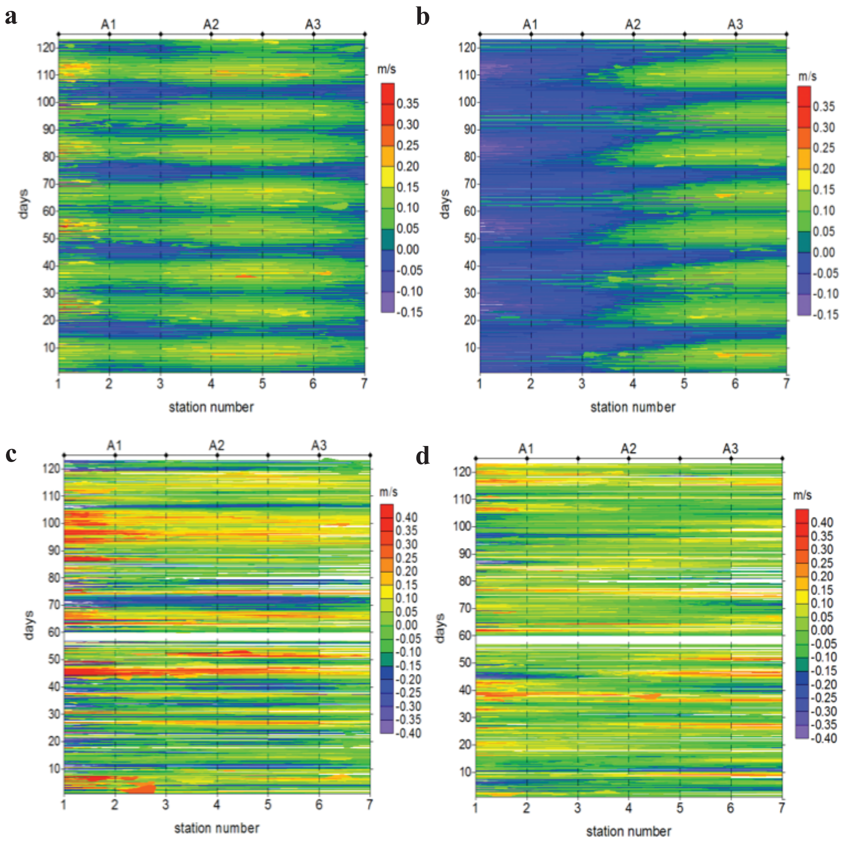

Fig. 11. Diagrams for sea currents observed at transect indicated in Fig. 2. The horizontal scale indicates pixel numbers 1–7 and the vertical scale shows time in days from the start (day 161) to the end of our experiment (day 284). Panels **a** and **b** present reconstruction of tidal current components u and v, respectively. Panels **c** and **d** illustrate u and v components of residual currents, respectively.

The dimensions of these tidal current ellipses, *i.e.* the semi-major and the semi-minor axes, are exaggerated in comparison to the spatial scale of the map, in order to obtain ellipses that are plainly visible to the reader. The grid points on the map are located 750 m apart. The dimensions of selected ellipses can be compared in Table 2. As seen in Fig. 13, at some locations (X4, A3), the tidal currents can be reversing. This means that the tidal flow alternates between approximately opposite directions with a short period of little or no tidal current. During the tidal flow in each direction, the current speed varies from zero to a maximum.

Example rotary spectra for observed surface currents and residual currents are shown in Fig. 14. For convenience, the spectra are plotted as a function of period, expressed in days. This example presents spectra obtained for station A1. The main features of rotary spectra estimated at other locations were similar (not

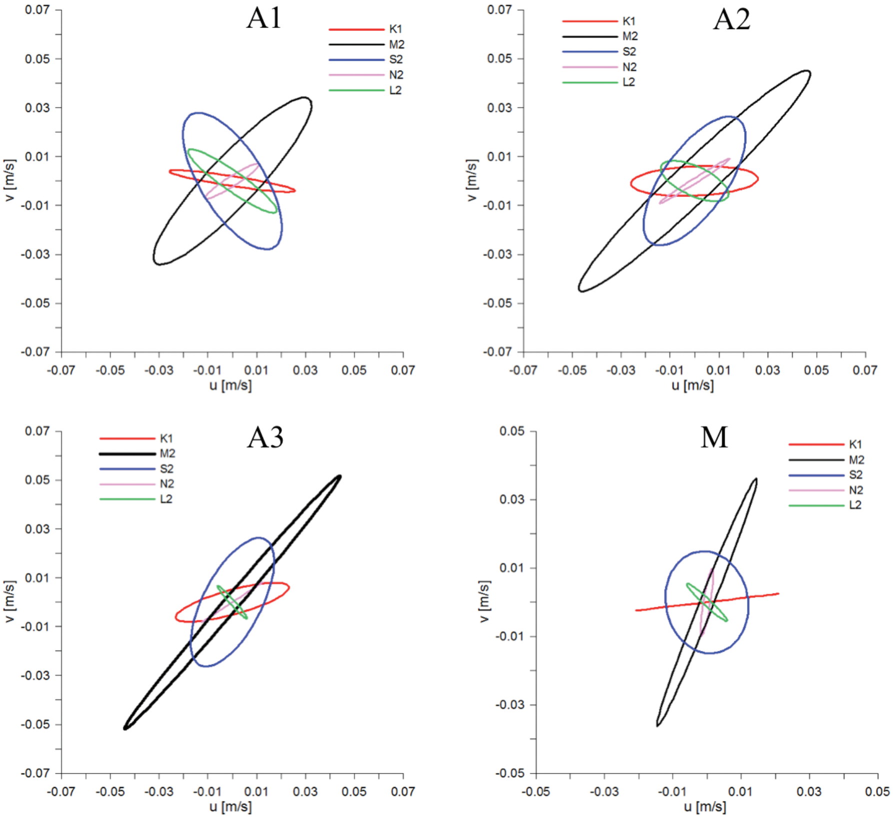

Fig. 12. Tidal ellipses illustrating the relative contribution of the most important tidal components to tidal currents at pixels A1, A2, A3, and M (see Fig. 2 for pixel positions).

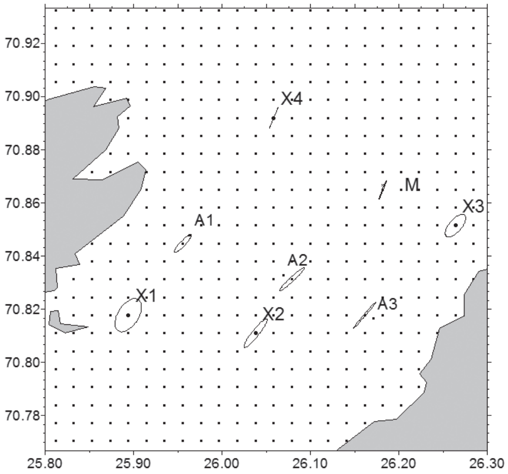

Fig. 13. Spatial distribution of M2 ellipses. The dimensions of selected ellipses are given in Table 2.

Table 2

Summary of the results from the tidal analysis of surface currents. Clockwise rotation is indicated by the minus sign for the semi-minor axis, inclination is the angle between east and the major axis of the ellipse.

STATION A1, depth ~ 170 m

| Constituent | Phase (degrees) | Major (m/s) | Minor (m/s) | Inclination (degrees) |
|---|---|---|---|---|
| M2 | 323.5 | 0.046 | -0.010 | 46.7 |
| S2 | 189.0 | 0.032 | -0.013 | 122.3 |
| N2 | 245.5 | 0.013 | 0.002 | 32.3 |
| L2 | 180.4 | 0.022 | -0.004 | 145.2 |
| K1 | 119.8 | 0.026 | -0.002 | 171.2 |

STATION A2, depth ~ 200 m

| Constituent | Phase (degrees) | Major (m/s) | Minor (m/s) | Inclination (degrees) |
|---|---|---|---|---|
| M2 | 335.2 | 0.065 | -0.008 | 43.6 |
| S2 | 227.2 | 0.031 | -0.013 | 54.5 |
| N2 | 292.8 | 0.017 | -0.001 | 32.4 |
| L2 | 175.7 | 0.015 | -0.006 | 155.5 |
| K1 | 295.6 | 0.026 | -0.006 | 2.5 |

STATION A3, depth ~ 200 m

| Constituent | Phase (degrees) | Major (m/s) | Minor (m/s) | Inclination (degrees) |
|---|---|---|---|---|
| M2 | 335.1 | 0.068 | -0.003 | 49.6 |
| S2 | 227.3 | 0.029 | -0.012 | 62.4 |
| N2 | 312.4 | 0.015 | -0.000 | 33.1 |
| L2 | 213.7 | 0.009 | 0.001 | 131.9 |
| K1 | 298.7 | 0.024 | -0.005 | 15.4 |

STATION M, depth ~ 210 m

| Constituent | Phase (degrees) | Major (m/s) | Minor (m/s) | Inclination (degrees) |
|---|---|---|---|---|
| M2 | 332.4 | 0.039 | -0.002 | 68.2 |
| S2 | 217.2 | 0.015 | -0.012 | 100.6 |
| N2 | 310.5 | 0.010 | 0.001 | 80.7 |
| L2 | 232.7 | 0.008 | 0.001 | 137.2 |
| K1 | 301.2 | 0.021 | 0.000 | 6.7 |

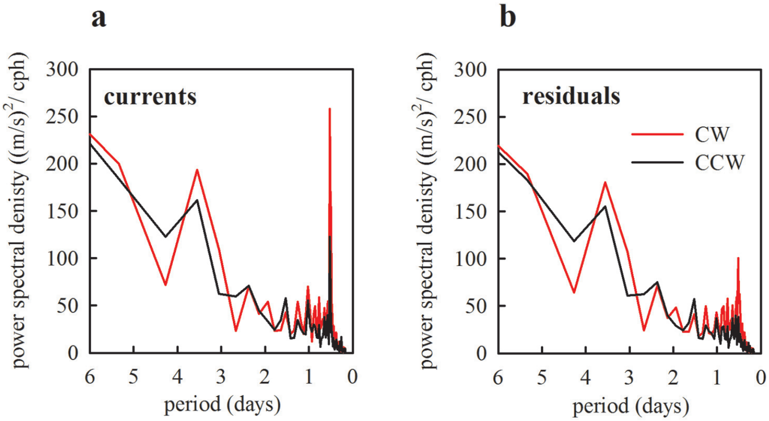

Fig. 14. Example rotary power spectra at location A1: (**a**) HF radar recorded current velocities, (**b**) current residuals. The red line indicates clockwise rotation and the black line indicates counterclockwise rotation.

shown). As can be seen on Fig. 14a, the most prominent peak for surface currents time series is observed at semidiurnal frequency. It is impossible to separate different tidal current constituents that are contributing to this peak in Fig. 14. This is because our observational time series were recorded at too low (hourly) temporal resolution to resolve these time scales through spectral analysis. In Fig. 14a, the peak for the diurnal variability is much smaller than the semidiurnal peak, in agreement with the results from harmonic analysis. If we compare Figs 14a and b, we note that the diurnal peak has been removed by the harmonic analysis. The semidiurnal peak is still present in the residual time series (Fig. 14b), although it is significantly smaller than in Fig. 14a, and is basically restricted to CW rotation. This shows that our harmonic tidal analysis has disassociated, at least to some degree, semidiurnal inertial currents from semidiurnal tidal currents.

In addition, we note that significant variance in the power spectrum is allocated to periods longer than diurnal, which is also seen in Fig. 15. Figure 15 compares power spectral densities for sea level and wind speed recorded in Honningsvaag, and current speed at station A1. In each case, the power spectrum has been normalized to the total variance of the respective time series. The plots show that relatively larger portion of the total variance is attributed to the diel and semidiurnal variability of sea level, than in the surface current speed time series. The corresponding maxima in the power spectrum for surface current speed are much less pronounced than in the power spectrum for sea level. Power spectra for wind and current speed indicate that proportionally more variance is attributed to time scales longer than a day, in comparison to the sea level data.

Figure 15b summarizes the results of the cross-spectral analysis between selected pairs of variables. Red line indicates the squared coherence between the wind and the current speed and blue line indicates the squared coherence

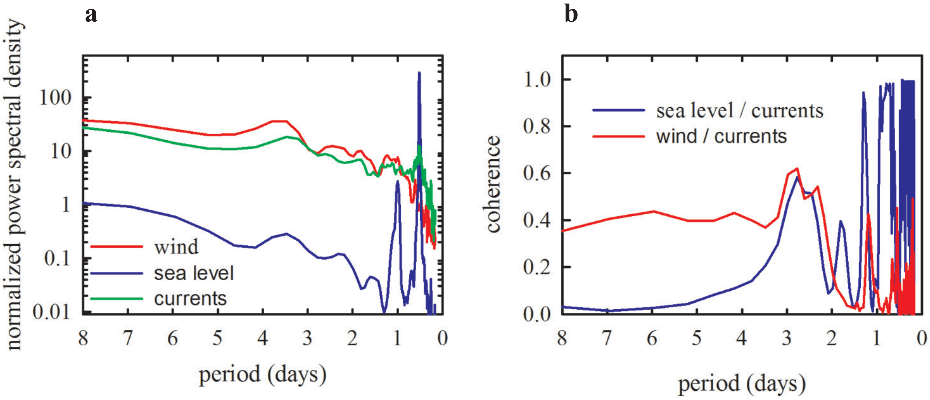

Fig. 15. (**a**) Comparison of the normalized power spectral density for wind speed, sea level, and surface current speed. Power spectra are normalized to the total variance. (**b**) Squared coherence between sea level and current speed (blue line) and between wind speed and current speed (red line) at location A1. The coherence >0.283 is significant at 95% confidence level.

between the sea level and the current speed, respectively. The coherence above 0.28 is statistically significant at 95% level (Bloomfield 2000; Bendat and Piersol 2011). In case of an ideal linear system the coherence would be one. We can see that the coherence between the wind speed and the current speed is above the critical level for periods longer than about 2.5 days and indicates that these variables are significantly correlated at synoptic time scales. In contrast, the sea level and the current speed are not significantly correlated at time scales longer than ~3.5 days, although there is a significant correlation at time scale of ~2–3 days. This can likely be related to atmospheric pressure variability. These results support the notion that adding to the complexity of the surface currents in the Porsanger fjord is the temporal and spatial variability of the wind's influence. Strong nontidal surface flows driven by wind stress are a very important contribution to the observed variability of surface currents.

Continuous observations of surface currents allowed us to estimate the average transport of surface waters across transect indicated by pixels S1–S7. The results are displayed in Fig. 16. Figure 16a shows time series of daily averaged transport estimated at each segment of the transect, as well as the total transport integrated between pixels S1 and S7. Figure 16b illustrates spatial distribution of water transport, expressed as $m^3$ of water transported during a day through 1 m of transect, on a 2D diagram. There are events when more surface water during the day is transported into than out of the fjord. The export of surface water from the fjord is more efficient on the south-eastern side of the fjord. However, on average the total daily transport of surface water out of the fjord is positive, and during our experiment it was estimated at about $32 \cdot 10^6$ $m^3$ per day

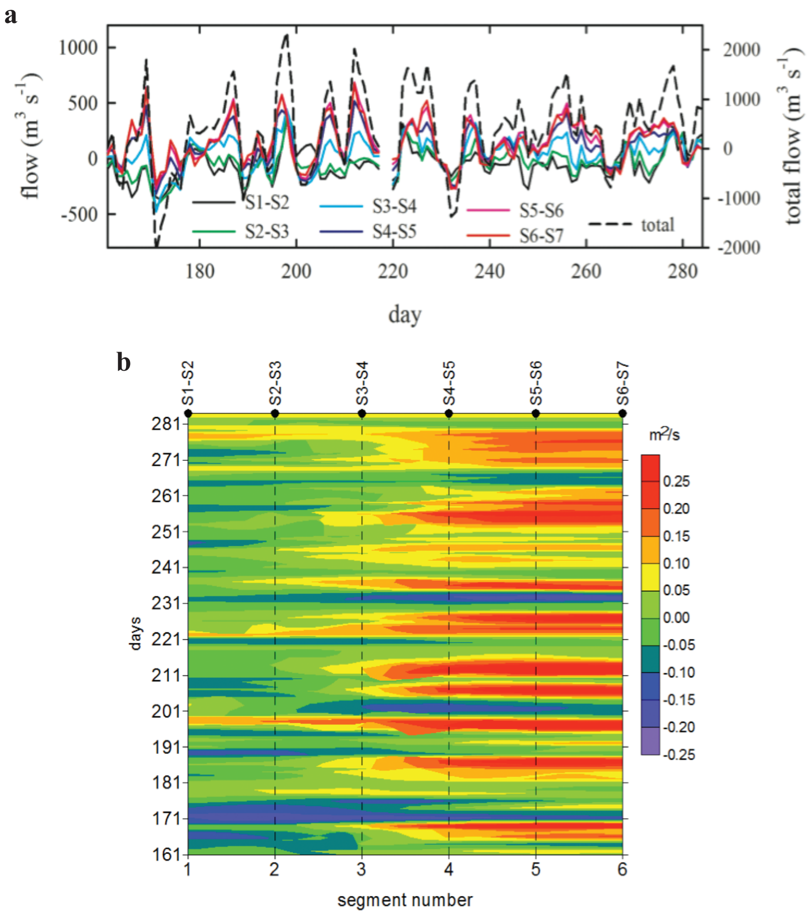

Fig. 16. Estimated daily averaged net transport of surface water across the transect shown in Fig. 2. (**a**) Time series of water transport at each of the segments of the transect and the total transport integrated across the transect line, and (**b**) 2-D diagram summarizing water transport.

assuming surface water layer 1-m thick. Obtaining an estimate of the total water transport at different water depths would require information about 3D flow in the fjord that is not available from the HF radar data.

## Summary

In this paper, we provided detailed information about surface currents in the Porsanger fjord. Tides are quite considerable, with tidal range on the order of about 3 m. Tidal analysis attributes to tides about 99% of variance in sea level time series recorded in Honningsvaag. The most important tidal component based on sea level data is the M2 component (amplitude of ~90 cm). The S2 and N2 components (amplitude of ~20 cm) also play a significant role in the semidiurnal sea level oscillations. The most important diurnal component is K1 with amplitude of about 8 cm.

Tidal analysis has led us to the conclusion that the most important tidal component in surface currents is the M2 component. The second most important is the S2 component. Our results indicate that in contrast to sea level, only about 10–30% of variance in surface currents can be attributed to tidal currents. This means that about 70–90% of variance can be credited to wind-induced and geostrophic currents. In particular, it is obvious that surface currents respond to the significant variability of wind including strong wind events. As a result, surface currents contain the component associated directly with wind forcing as well as the inertial component.

Our data did not allow us to achieve the necessary frequency resolution and to strictly separate the inertial oscillations from tidal variations. However, our results indicate that most of the variance in the time series of surface currents is allocated to time scales longer than diurnal. This indicates that surface currents in the fjord can have a significant component related to Ekman forcing.

Because of the complicated interactions involving wind field (variable in time and spatially) and topography of the fjord, we underline the need for further investigation of currents in this region using a coastal model. We plan to adapt such model and to further investigate various scales of ocean current variability observed with the HF radar system.

Finally, our data allowed us to estimate time series of surface water transport out of the fjord area monitored by the HF radar system. These results confirmed the general expectations that, on average, transport of surface waters out of the fjord dominates in this region. This transport has to be compensated by the inflow of oceanic waters at greater depth, as well as by the transport of fresh water from rivers and land runoff. Better understanding of the water budget will be possible through a modeling study.

**Acknowledgements**. — We are grateful to Thomas Helzel and his staff from Helzel Messtechnik GmbH for their support with all aspects of HF radar system operations. Many thanks to Knut Yngve Børsheim, Hans Kristian Strand, and Henrik Søiland from Institute of Marine Research for their help with the field logistics. We are grateful to Jagoda Białogrodzka, Dariusz Ficek, Mateusz Jakowczyk, Daniel Materka, Roman Majchrowski, Roman Marks, Marek Świrgoń, Marzena Wereszka, and Tomasz Żmójdzin for their participation in the NORDFLUX field experiment in 2014. The authors are grateful to all the persons involved in the programs providing free access to the data sets used in this study. The sea level data were provided by the Norwegian Hydrographic Service. Meteorological data from Honningsvaag were made available by the Norwegian Meteorological Institute. This work was funded by the Norway Grants through the Polish-Norwegian Research Programme operated by the National Centre for Research and Development NCBR contract No. 201985 *Application of in situ observations, high frequency radars, and ocean color, to study suspended matter, particulate carbon, and dissolved organic carbon fluxes in coastal waters of the Barents Sea*. Partial funding for MS and AJ comes also from the statutory funds at IO PAN. We would also like to thank Daniel C. Conley and an anonymous reviewer for their detailed and constructive comments which helped to improve this paper.

## References

BARTH A., ALVERA-AZCÁRATE A., GURGEL K.-W., STANEVA J., PORT A., BECKERS J.-M. and STANEV E.V. 2010. Ensemble perturbation smoother for optimizing tidal boundary conditions by assimilation of High-Frequency radar surface currents – application to the German Bight. *Ocean Science* 6: 161–178.

BENDAT J.S. and PIERSOL A.G. 2010. *Random Data: Analysis and Measurement Procedures*. Wiley, New York: 640 pp.

BLOOMFIELD P. 2000. *Fourier Analysis of Time Series: an Introduction*. Wiley, New York: 288 pp.

CARBAJAL N. and POHLMANN T. 2004. Comparison between measured and calculated tidal ellipses in the German Bight. *Ocean Dynamics* 54: 520–530.

CHAPMAN R.D., SHAY L.K., GRABER H.C., EDSON J.B., KARACHINTSEV A., TRUMP C.L. and ROSS D.B. 1997. On the accuracy of HF radar surface current measurements: Intercomparisons with ship based sensors. *Journal of Geophysical Research* 102: 18737–18748.

CUSHMAN-ROISIN B., ASPLIN L. and SVENDSEN H. 1994. Upwelling in broad fjords. *Continental Shelf Research* 14: 1701–1721.

EILERTSEN H.C. and FRANTZEN S. 2007. Phytoplankton from two sub-Arctic fjords in northern Norway 2002–2004: I. Seasonal variations in chlorophyll a and bloom dynamics. *Marine Biology Research* 3: 319–32.

FOREMAN M.G.G. 1977. (on line version revised in 2004). *Manual for tidal heights analysis and prediction*. Institute of Ocean Sciences, Patricia Bay, Sidney: 97 pp.

FOREMAN M.G.G. 1978. (on line version revised in 2004). *Manual for tidal currents analysis and prediction*. Institute of Ocean Sciences, Patricia Bay, Sidney: 57 pp.

GONELLA J. 1972. Rotary component method for analyzing meteorological and oceanographic vector time series. *Deep Sea Research* 19: 833–846.

GOOD S.A., CORLETT G.K., REMEDIOS J.J., NOYES E.J. and LLEWELLYN-JONES D.T. 2007. The global trend in sea surface temperature from 20 years of Advanced Very High Resolution Radiometer data. *Journal of Climate* 20: 1255–1264.

HELZEL T., KNIEPHOFF M. and PETERSEN L. 2010. Oceanography radar system WERA: features, accuracy, reliability and limitations. *Turkish Journal of Electrical Engineering and Computer Science* 18: 389–397.

HELZEL T., PETERSEN L., MARIETTE V. and PAVEC M. 2011. Reliability of Coastal Radar WERA for Coastal Zone Management. *Journal of Coastal Research* SI 64: 1345–1347.

JAKOWCZYK M. and STRAMSKA M. 2014. Spatial and temporal variability of satellite-derived sea surface temperature in the Barents Sea. *International Journal of Remote Sensing* 35: 6545–6560.

KAPLAN D.M., LARGIER J. and BOTSFORD L.W. 2005. HF radar observations of surface circulation off Bodega Bay (northern California, USA). *Journal of Geophysical Research – Oceans* 110: C10020.

KOHUT J.T. and GLENN S.M. 2003. Improving HF radar surface current measurements with measured antenna beam patterns. *Journal of Atmospheric and Oceanic Technology* 20: 1303–1316.

KOKKINI Z., POTIRIS M., KALAMPOKIS A. and ZERVAKIS V. 2014. HF Radar observations of the Dardanelles outflow current in North Eastern Aegean using validated WERA HF radar data. *Mediterranean Marine Science* 15: 753–768.

MAYER D.A., MOFJELD H. and LEAMAN K.D. 1981. Near-inertial internal waves observed on the outer shelf in the Middle Atlantic Bight in the wake of Hurricane Belle. *Journal of Physical Oceanography* 11: 87–106.

OHLMANN C., WHITE P. WASHBURN L., TERRILL E., EMERY B. and OTERO M. 2007. Interpretation of coastal HF radar derived surface currents with high resolution drifter data. *Journal of Atmospheric and Oceanic Technology* 24: 666–680.

PADUAN J.D. and GRABER H.C. 1997. Introduction to high-frequency radar: Reality and myth. *Oceanography* 10: 36–39.

PARKS A.B., SHAY L.K., JOHNS W.E., MARTINEZ-PEDRAJA J. and GURGEL K.-W. 2009. HF radar observations of small-scale surface current variability in the Straits of Florida. *Journal of Geophysical Research* 114: C08002.

ROBINSON A.M. and WYATT L.R. 2011. A two year comparison between HF radar and ADCP current measurements in Liverpool Bay. *Journal of Operational Oceanography* 4: 33–45.

SEALEN O.H. 1967. Some features of the hydrography of Norwegian fjords. *In:* G.H. Lauff (ed.) *Estuaries*. American Association for the Advancement of Science, Washington D.C., USA: 63–70.

SHAY L.K., SEIM H.E., SAVIDGE D., STYLES R. and WEISBERG R.H. 2008. High frequency radar observing systems in SEACOOS: 2002–2007 lessons learned. *Marine Technology Society Journal* 42: 55–67.

SIVERTSEN K. and BJØRGE A. 2015. On the brink of the Arctic: Unusual intertidal sub-Arctic kelp associations in the Porsangerfjord, North Norway. *Marine Biology Research* 11: 405–413.

STANEV E.V., ZIEMER F., SCHULZ-STELLENFLETH J., SEEMANN J., STANEVA J. and GURGEL K.-W. 2014. Blending Surface Currents from HF Radar Observations and Numerical Modeling: Tidal Hindcasts and Forecasts. *Journal of Atmospheric and Oceanic Technology* 32: 256–281.

SVENDSEN H. 1995. Physical oceanography of coupled fjord-coast systems in northern Norway with special focus on frontal dynamics and tides. *In*: H. Skjoldal, C. Hopkins, K. Erikstad, H. Leinaas (eds) *Ecology of Fjords and Coastal Waters*. Elsevier, Amsterda, New York: 149–164.

WUNSCH C. 1975. Internal tides in the ocean. *Reviews of Geophysics and Space Physics*, 13: 167–182.

Received 14 April 2016
Accepted 11 July 2016